IOP Publishing | Institute of Physics and Engineering in Medicine Physics in Medicine & Biology

Phys. Med. Biol. **60** (2015) 8249–8274 doi:10.1088/0031-9155/60/21/8249

Rapid MCNP simulation of DNA double strand break (DSB) relative biological effectiveness (RBE) for photons, neutrons, and light ions

Robert D Stewart[1], Seth W Streitmatter[2], David C Argento[1], Charles Kirkby[3,4,5], John T Goorley[6], Greg Moffitt[2], Tatjana Jevremovic[2] and George A Sandison[1]

[1] Department of Radiation Oncology, University of Washington School of Medicine, School of Medicine, 1959 NE Pacific Street, Box 356043, Seattle, WA 98195, USA
[2] The University of Utah, Nuclear Engineering Program (UNEP), 50 S. Central Campus Drive, Salt Lake City, UT 84112, USA
[3] Jack Ady Cancer Centre, Lethbridge, Alberta, Canada
[4] Department of Physics and Astronomy, University of Calgary, Tom Baker Cancer Centre, Calgary, Alberta, Canada
[5] Department of Oncology, University of Calgary, Tom Baker Cancer Centre, Calgary, Alberta, Canada
[6] Los Alamos National Laboratory, X Computational Physics Division, Mailstop A143, Los Alamos, NM 87505, USA

E-mail: trawets@uw.edu

Received 4 March 2015, revised 11 August 2015
Accepted for publication 1 September 2015
Published 9 October 2015

Abstract

To account for particle interactions in the extracellular (physical) environment, information from the cell-level Monte Carlo damage simulation (MCDS) for DNA double strand break (DSB) induction has been integrated into the general purpose Monte Carlo N-particle (MCNP) radiation transport code system. The effort to integrate these models is motivated by the need for a computationally efficient model to accurately predict particle relative biological effectiveness (RBE) in cell cultures and *in vivo*. To illustrate the approach and highlight the impact of the larger scale physical environment (e.g. establishing charged particle equilibrium), we examined the RBE for DSB induction (RBE_{DSB}) of x-rays, ^{137}Cs γ-rays, neutrons and light ions relative to γ-rays from ^{60}Co in monolayer cell cultures at various depths in water. Under normoxic conditions, we found that ^{137}Cs γ-rays are about 1.7% more effective at creating DSB than γ-rays from ^{60}Co ($RBE_{DSB} = 1.017$) whereas 60–250 kV x-rays are 1.1 to 1.25 times more efficient at creating DSB than

^{60}Co. Under anoxic conditions, kV x-rays may have an RBE_{DSB} up to 1.51 times as large as ^{60}Co γ-rays. Fission neutrons passing through monolayer cell cultures have an RBE_{DSB} that ranges from 2.6 to 3.0 in normoxic cells, but may be as large as 9.93 for anoxic cells. For proton pencil beams, Monte Carlo simulations suggest an RBE_{DSB} of about 1.2 at the tip of the Bragg peak and up to 1.6 a few mm beyond the Bragg peak. Bragg peak RBE_{DSB} increases with decreasing oxygen concentration, which may create opportunities to apply proton dose painting to help address tumor hypoxia. Modeling of the particle RBE for DSB induction across multiple physical and biological scales has the potential to aid in the interpretation of laboratory experiments and provide useful information to advance the safety and effectiveness of hadron therapy in the treatment of cancer.

Keywords: RBE, DSB, MCNP, MCDS, ions, neutron, photon biology

(Some figures may appear in colour only in the online journal)

Introduction

The safe and effective delivery of therapeutic radiation for the treatment of cancer, as well as the accurate prediction of the biological consequences of exposure to ionizing radiation during imaging procedures and as a consequence of occupational, natural or accidental exposures, depends on accurate dosimetry and, in many cases, an accurate assessment of the biological effectiveness of one type of radiation relative to another. Conceptually, the relative biological effectiveness (RBE) of a radiation is the absorbed dose of a (usually) low linear energy transfer (LET) reference radiation, such as γ-rays from ^{60}Co, that produces a biological effect (endpoint) E divided by the absorbed dose of an alternate (often higher LET) radiation that produces the same effect E. In this work, we have developed a computationally efficient framework to accurately predict the RBE for DNA double strand break (DSB) induction across multiple biological scales (cell to tissue levels). Because the biological processing of DSB into chromosome aberrations is a central mechanism underlying cell reproductive death (Cornforth and Bedford 1987, Bedford 1991, Hlatky *et al* 2002, Carlson *et al* 2008, Stewart *et al* 2011) and oncogenic transformation (Obe *et al* 2002, Rothkamm and Lobrich 2002, Worku *et al* 2013, Byrne *et al* 2014), the RBE for DSB induction (RBE_{DSB}) may be useful as a molecular surrogate in studies of radiation carcinogenesis and in the biological optimization of hadron therapy for the treatment of cancer. As a first approximation, the effects of particle LET and oxygen concentration on the linear-quadratic (LQ) model parameters α and β are related to RBE_{DSB} by $\alpha_{ion} \cong \alpha_\gamma \cdot RBE_{DSB}$ and $\sqrt{\beta_{ion}} \cong RBE_{DSB} \cdot \sqrt{\beta_\gamma}$ (Stewart *et al* 2011). Here, the subscript γ denotes the LQ parameter for a low LET reference radiation (e.g. γ-rays from ^{60}Co), and the subscript *ion* denotes a charged particle or other test radiation of interest.

The Monte Carlo damage simulation (MCDS) developed by Stewart and colleagues (Semenenko and Stewart 2004, 2006, Stewart *et al* 2011) quickly generates nucleotide-level maps of the clusters of DNA lesions formed by electrons and light ions up to ^{56}Fe. MCDS estimates of the number of DSB and other simple and complex clusters of DNA lesions are

in good agreement with event by event track structure simulations (Nikjoo *et al* 1997, 1999, 2001, Friedland *et al* 2003, Campa *et al* 2009, Alloni *et al* 2010) and measurements (Stewart *et al* 2011 and references therein). For monoenergetic charged particles, Monte Carlo simulation of DNA damage in 10 000 mammalian cells, which usually suffices to estimate the mean number of DSB Gy^{-1} Gbp^{-1} with a standard error of the mean better than 0.2%, typically only requires about 1 min of CPU time on a fast[7] desktop computer. Cell-level simulations of a radiation field composed of a mixture of particle types are more CPU intensive, i.e. ~1 min per particle type and energy. Although the MCDS includes a sub-cellular dosimetry model for charged particles passing through water (Stewart *et al* 2011), the interactions of particles in the larger-scale extracellular and physical environment must be simulated using a general purpose radiation transport model such as PENELOPE (Hsiao and Stewart 2008, Kirkby *et al* 2013, Hsiao *et al* 2014), MCNPX or the newer MCNP6 (Ezzati *et al* 2015) or FLUKA (Wang *et al* 2012). Larger scale simulations are also needed to compute dose-averaged RBE values in a region of interest, such a 1–100 mm^3 computed tomography (CT) voxel, or over an entire organ, tissue or tumor target.

To enable more efficient Monte Carlo simulations of DNA damage on the multi-cellular and larger tissue scales, we first used the MCDS to estimate the RBE for DSB induction (RBE_{DSB}) relative to ^{60}Co γ-rays as well as the numbers of DSB Gy^{-1} Gbp^{-1} for electrons and light ions up to and including ^{56}Fe. We then fit the RBE estimates from the MCDS to analytic formulas that cover the entire range of particle types and energies. Separate formulas are reported for cells irradiated under anoxic and normoxic (O_2 concentration greater than about 5–7%) conditions. The reported empirical formulas are a convenient way to summarize a large body of data and serve as a useful benchmark for the intercomparison of DSB estimates from measurements, analytic formulas (Van den Heuvel 2014) and Monte Carlo simulations (Holley and Chatterjee 1996, Nikjoo *et al* 1997, 1999, 2001, 2002, Friedland *et al* 2003, Bernal *et al* 2011, Pater *et al* 2014). Empirical formulas are also potentially useful for the rapid recording (scoring or tallying) of the product of dose $\times$ RBE (i.e. the biologically equivalent ^{60}Co dose).

To illustrate the effects of charged particle equilibrium (CPE) and other effects of particle interactions in the larger-scale physical environment, we used dose–response (RBE_{DSB}) lookup tables in the Monte Carlo N-particle (MCNP) code system Version 6.1 (Goorley *et al* 2013) to examine the biological equivalence of selected low linear energy transfer (LET) radiations often used as the reference radiation in particle RBE experiments. We also used this approach to estimate from first principles the RBE for DSB induction of monoenergetic neutrons (1 keV to 100 MeV), fission neutrons (^{232}Th, ^{235}U, ^{238}U, ^{239}Pu, ^{240}Pu, ^{242}Cm, ^{244}Cm, and ^{252}Cf) and the University of Washington Clinical Neutron Therapy System (CNTS) fast neutron beam (50.5 MeV $^{1}H^{+}$ ions incident on a Be target). Because of the expanding number of proton therapy facilities in the US and abroad, we also used MCNP to examine spatial variations in proton RBE within representative pencil beams relevant to radiation therapy. Although this paper focuses on the endpoint of DSB induction, the presented examples provide useful information on trends in the RBE of neutrons, photons and light ions for an important molecular endpoint and highlights issues relevant to the design of future *in vitro* and *in vivo* experiments for other endpoints, such as the effects of filtration on the RBE of low energy x-ray reference radiations and the effects of beam hardening and CPE with depth into water or a patient.

[7] 2.53 GHz Intel(R) Xeon(R) CPU, 24 GB RAM, 64-bit Microsoft Windows 7 processor score of 7.7.

Materials and methods

Generation of DNA damage in the MCDS

Clusters of DNA lesions generated by ionizing radiation are typically composed of one or a few individual DNA lesions (damaged nucleotides) formed within one or two turns of the DNA. Because the initial direct and indirect physiochemical reactions responsible for the creation of a cluster of DNA lesions are localized within volumes not larger than about 10 nm, the MCDS simulates damage induction in a small segment of a DNA molecule uniformly irradiated by monoenergetic charged particles. Damage within that segment is then scaled in direct proportion to the total amount of DNA in a cell, or conversely, reported as the number of clusters per unit absorbed dose per unit length of DNA. In general, the MCDS simulates the induction of damage using a two-step algorithm. First, the expected number of individual lesions (damaged nucleotides) that would occur per gigabase pair (Gbp) of DNA from the delivery of 1 Gy of monoenergetic radiation in the presence of a defined oxygen concentration is randomly distributed across a small DNA segment. Second, lesions within the DNA segment are grouped into one of three mutually exclusive categories of cluster (single strand break (SSB), DSB, and clusters composed only of base damage). Within each major category of damage, the numbers of each type of cluster are also tallied using metrics indicative of cluster complexity, such as the number of lesions forming the cluster.

The algorithm used within the MCDS has three adjustable (*input*) parameters (σ_{Sb}, f, n_{min}) that are, as a good first approximation, independent of the charged particle type and kinetic energy and one parameter (n_{seg}) that depends on particle type and kinetic energy. Here, n_{seg} is the length of a segment of DNA in base pairs (bp), σ_{Sb} is the number of individual strand breaks per unit dose per amount of DNA in the cell (*not* the DNA segment), f is the ratio of base damage to strand breaks ~3 (the number of nucleotides in the DNA segment with base damage is $f\sigma_{\mathrm{Sb}}$), and n_{min} is the minimum length (in bp) of undamaged DNA (in bp) such that adjacent lesions in the same or opposed DNA strands are considered part of different clusters. The ratio of three damaged bases per strand break ($f = 3$) is the same as the value used in recent track structure simulations of non-DSB clusters (Watanabe *et al* 2015). For charged particles with kinetic energy T, the n_{seg} parameter is computed as (Semenenko and Stewart 2006)

$$n_{\mathrm{seg}}(x) = 149\,200 - \frac{123600(x)}{(x + 267)} \quad \text{(base pairs)}$$
$$\text{where } x = \left[1 - \frac{1}{1 + \frac{T}{m_0c^2}}\right]^{-1}. \tag{1}$$

Here, m_0c^2 is the rest mass of an electron. The specific mathematical form of equation (1) was determined from an empirical fit of the numbers of SSB and DSB from the MCDS (Semenenko and Stewart 2006) to the results from track structure simulations (Nikjoo *et al* 1994, 1997, 1999, 2001, 2002, Friedland *et al* 2003, 2005) for electrons, protons and alpha particles.

Effects of radical scavenging and bystander effects in MCDS simulations

The conceptual model used to simulate DNA damage in the MCDS is premised on the conventional dogma that ionizing radiation damages the DNA through the direct ionization or excitation of the DNA and through the indirect action of hydroxyl or other radicals formed in close proximity to the DNA. However, there are many reports in the literature of cellular and genetic

damage arising from extracellular signals, i.e. the so-called bystander and non-targeted effects of radiation (Mothersill and Seymour 1998, Morgan 2003a, 2003b, Wright and Coates 2006, Wright 2010). Although the MCDS does not explicitly distinguish DNA damage arising from extracellular signaling in adjacent or nearby cells from damage induced from smaller-scale (<5–10 nm) physiochemical mechanisms, the aggregate effects of direct and *all* indirect DNA damage mechanisms are ultimately embedded (*implicit*) in the values selected for the σ_{Sb} and f parameters. Because the default parameters used in the MCDS were primarily selected to reproduce measured data from cell culture and other experiments (Stewart *et al* 2011 and references therein), the MCDS implicitly accounts for DNA damage arising from intra- and extracellular signals in adjacent and nearby *irradiated cells*, e.g. the overall levels of DNA damage observed in a uniformly irradiated monolayer cell culture. Although the MCDS has the ability to separate DNA damage arising from the direct and indirect mechanisms through simulations of the effects of radical scavengers (Semenenko and Stewart 2006), the MCDS does not have any means to separate DNA damage arising from extracellular signaling from damage arising through indirect, subcellular mechanisms. DNA damage arising in non-irradiated ('bystander') cells from extracellular signals generated by (released from) irradiated cells are neglected in the MCDS.

Relationship of the MCDS to track structure simulations of DNA damage

Track structure simulations of the induction of DNA damage by ionizing charged particles (Holley and Chatterjee 1996, Nikjoo *et al* 1997, 1999, 2001, Ballarini *et al* 2000, Bernhardt *et al* 2002, Friedland *et al* 2002, 2003, Campa *et al* 2005, Alloni *et al* 2013) begins with a detailed physical model of the interactions of a particle passing through a liquid medium, usually water. Then, the locations of individual energy transfer events (ionization and excitation) along the trajectory of the ion, as well as any secondary charged particles formed by the primary ion, are typically superimposed on a model of the DNA and chromatin. Energy deposition events that directly involve (coincide with) a nucleotide, or the phosphodiester bond linking adjacent nucleotides, are damaged with a certain probability to form individual strand breaks or base damage, i.e. the *direct DNA damage mechanism*. The formation of strand breaks and base damage through the direct effect is often parameterized by introducing an energy threshold on the order of a few tens of eV (Nikjoo *et al* 2001). Energy deposition events in the DNA larger than the threshold produce a DNA lesion (strand break or base damage) whereas smaller energy deposition events do not. Alternatively, a linear or other simple function may be used to relate the size of an energy deposit to lesion induction through the direct mechanism (Holley and Chatterjee 1996, Friedland *et al* 2003).

To model the formation of individual lesions from the *indirect damage mechanism*, analog Monte Carlo simulations (Ballarini *et al* 2000, Kreipl *et al* 2009, Alloni *et al* 2013) or simple probability models are used to mimic the diffusion and interactions of hydroxyl (·OH) or other radicals with the DNA. Models of the indirect action of radiation typically require the introduction of at least one or two additional parameters, such as a parameter to relate indirect (radical-mediated) hits on a nucleotide to the formation of a strand break and another parameter to relate 'hits' to base damage. For example, a ·OH formed within about 4–6 nm of a nucleotide has a 0.13 chance of creating a strand break (Nikjoo *et al* 1999, 2001). Similar probability models are used to determine the chance a base is damaged by an ·OH.

An appealing aspect of the track structure simulation approach to modeling DNA damage is that the clustering of two or more individual DNA lesions to form a DSB, or other complex cluster of DNA lesions, arises as a direct consequence of the ionization density (spatial

distribution of energy deposits) on a nanometer scale. The parameters and probability models used to relate the spatial distribution of energy deposits to the formation of individual and clusters of DNA lesions are presumably the same for all types of low and high LET radiations. The structure of the track is determined from the physical interactions of the charged particle with the medium and can be considered free of *ad hoc* adjustable parameters for most purposes. Any effects on the clustering of lesions associated with the higher order structure of the DNA and chromatin arise from the larger-scale features of the track as an ion passes through the cell nucleus.

In the MCDS, the σ_{Sb} and f parameters quantify the initial numbers of individual lesions formed per unit dose of radiation and per unit length of DNA. These parameters serve the same role in the MCDS as the energy thresholds and probability models used in track structure simulations to relate the magnitude of an energy deposition event in or near the DNA to the formation of individual DNA lesions. As in track structure simulations, the MCDS treats the σ_{Sb} and f parameters as independent of particle type and LET (kinetic energy). The most significant difference between the MCDS and analog track structure simulations relates to the conceptual model/algorithm used in the placement of individual lesions within the DNA to form clusters of DNA lesions, such as a DSB or complex SSB (e.g. a strand break with base damage in opposed DNA strand). In the MCDS, the placement of individual lesions to form a cluster is indirectly controlled in the MCDS by inserting a fixed number of individual lesions at random into a DNA segment of varying length. The length of the DNA segment depends on the particle type and energy, i.e. the n_{seg} parameter as defined by equation (1). Large DNA segments correspond to low LET radiations (high-energy charged particles) and small DNA segments correspond to high LET (low-energy charged particles).

The *ad hoc* seeming method used in the MCDS to control the cluster of lesions within the DNA arose as a fortuitous byproduct of an independent effort to simulate the base and nucleotide excision repair of clusters of DNA lesions other than the DSB (Semenenko and Stewart 2005, Semenenko *et al* 2005). The accuracy and ultimate outcome from the attempted excision repair of a cluster and DNA lesions (other than a DSB) is critically dependent on the spatial distribution, orientation (same or opposed DNA strand) and the types of lesions (base damage or strand break) within one or two turns of the DNA (~10 to 20 base pairs). The algorithm used for lesion clustering in the MCDS (Semenenko and Stewart 2004) was initially considered no more than a computationally efficient way to generate representative configurations of clusters of DNA lesions to serve as an input into the Monte Carlo excision repair (MCER) model (Semenenko and Stewart 2005, Semenenko *et al* 2005). However, the simple lesion clustering algorithm used in the MCDS reproduces the numbers of SSB and DSB as well as the relative numbers of eight other categories of simple and complex DNA clusters (SSB+, 2 SSB, DSB+, DSB++, SSB_c, SSB_{cb}, DSB_c, DSB_{cb}) with surprising accuracy (Semenenko and Stewart 2004, 2006, Stewart *et al* 2011). The algorithm used in the MCDS has also been adapted to simulate the effects of radical scavengers (Semenenko and Stewart 2006), the interplay between particle LET and the concentration of oxygen present at the time of irradiation, and the formation of Fpg and Endo III clusters (Stewart *et al* 2011). We have also shown through combined MCDS + MCER simulations that trends in the numbers of HPRT mutations and the numbers of DSB formed through the aborted (incomplete) excision repair of non-DSB clusters are in good agreement with measurements (Semenenko and Stewart 2005, Semenenko *et al* 2005).

The successes of the MCDS at reproducing measurements and the results of analog track structure simulations may point to a simplified, but perhaps equally fundamental, conceptual model for the way clusters of DNA lesions are formed on a nanometer scale (few turns of the DNA). Namely, the distribution of individual lesions formed within one or two turns of the

DNA (i.e. on the spatial scale in which clusters are created) is governed by a stochastic process that is largely determined by the number of DNA lesions formed per unit length of DNA. In the MCDS, the number of lesions per unit length of DNA is determined by the σ_{Sb}, f and n_{seg} parameters. The tendency towards increasing levels of lesion clustering as particle LET increases arises because the number of lesions per unit length of DNA increases with increasing LET (σ_{Sb} and f are constant and n_{seg} tends to decrease with increasing LET).

For the scheme used in the MCDS to be considered more than an empirical tool to reproduce the results of track structure simulations, all nucleotides within about one or two turns of the DNA (~10 to 20 bp) must be about equally likely to be damaged through the direct and indirect action of ionizing radiation. As conceptual motivation for this approach, consider a linear section of DNA 10 bp in length (i.e. ~length in bp of a DSB composed of exactly two opposed strand breaks) occupying a cylindrical volume not larger than about than 2 nm in diameter and 3 nm in length (~0.3 nm per bp), i.e. ~10 nm^3. Because the orientation and packaging of this small segment of DNA is independent of the (*random*) trajectory of an ion (and the secondary electrons created by the primary), it is reasonable to assume that all 20 nucleotides (=10 bp) in a 10 nm^3 are about equally likely to sustain damage from the direct mechanism. As a first approximation, it also seems quite reasonable to assume that nucleotides within a 10 nm^3 region of interest are about equally likely to be indirectly damaged because the average distance an ·OH can diffuse in a cellular environment is on the order of 4–6 nm (Roots and Okada 1975, Goodhead 1994, Nikjoo *et al* 1997, Georgakilas *et al* 2013), i.e. the same order of magnitude as the dimensions of the molecular domain of interest for cluster formation (~10 nm^3). To the extent that all nucleotides within a region of interest associated with the formation of a cluster of DNA lesions (~10 nm^3) are about equally likely to be damaged, the MCDS can be considered a simple but still mechanistic alternative to track structure simulations. The σ_{Sb} and f parameters relate the deposition of energy (dose) to the numbers of individual lesions, and n_{seg} parameterizes the effects on lesion clustering of differences in track structure and ionization density.

MCDS estimates of RBE_{DSB} for electron and light ions

We used the MCDS Version 3.10A (Stewart *et al* 2011) to generate estimates of the number of DSB Gy^{-1} Gbp^{-1} for selected monoenergetic electrons and light ions (i.e. e^-, $^1H^+$, $^4He^{2+}$, $^{12}C^{6+}$, and $^{56}Fe^{26+}$) with $(z_{eff}/\beta)^2$ as large as 2×10^5. Large values of $(z_{eff}/\beta)^2$ correspond to low energy, high linear energy transfer (LET) particles. For very high energy ions, the speed β of the ion relative to the speed of light approaches unity, and the effective charge approaches Z (Barkas and Evans 1963), i.e.

$$z_{eff} = Z\left[1 - \exp(-125 \cdot \beta \cdot Z^{-2/3})\right], \tag{2}$$

and

$$\beta = \sqrt{1 - \frac{1}{(1 + T/m_0c^2)^2}}. \tag{3}$$

Here, T is the kinetic energy of the charged particle (in MeV), and m_0c^2 is the rest mass energy of the charged particle (in MeV).

All of the reported results, as well as results reported in numerous other publications (Semenenko and Stewart 2006, Reniers *et al* 2008, Stewart *et al* 2011, Neshasteh-Riz *et al* 2012, Wang *et al* 2012, Hsiao *et al* 2014, Pater *et al* 2014, Van den Heuvel 2014, Polster *et al* 2015), are based on the default MCDS parameter values ($\sigma_{Sb} = 217$ Gy^{-1} Gbp^{-1}, $f = 3$,

$n_{\min} = 9$ bp), which have been shown to adequately reproduce cluster yields for a wide range of particle types, kinetic energies and oxygen concentrations (Stewart *et al* 2011 and references therein). All MCDS simulations are for a minimum of 10 000 cells (standard error of the mean $\leqslant 0.2\%$). MCDS simulations were performed for cells irradiated under normoxic conditions (O_2 concentration $\geqslant 8\%$) and anoxic conditions (0% O_2). The effects of O_2 concentration on DSB induction are negligible beyond about 8% (figure 2 in Stewart *et al* 2011).

We computed the RBE for DSB induction relative to ^{60}Co γ-rays by dividing the number of DSB Gy^{-1} Gbp^{-1} for the ion of interest by the number of DSB Gy^{-1} Gbp^{-1} for cells irradiated by ^{60}Co γ-rays *in vitro* (8.32 DSB Gy^{-1} Gbp^{-1} normoxic cells, 2.86 DSB Gy^{-1} Gbp^{-1} anoxic cells). For comparison to measurements or simulations in which a radiation other than ^{60}Co is used as the reference radiation, the estimates of RBE_{DSB} relative to ^{60}Co reported in this work should be multiplied by the DSB yield of ^{60}Co and divided by the DSB yield of the desired reference radiation. For example, 125 kVp x-rays produce about 1.11 times as many DSB as ^{60}Co γ-rays (Kirkby *et al* 2013). Therefore, estimates of the RBE reported in this work would need to be divided by 1.11 to use 125 kVp x-rays as the reference radiation. See also table 2 in this work for the RBE of other selected, low LET reference radiations.

Empirical formulas for RBE_{DSB}

The TableCurve 2D Version 5.01 (SYSTAT Software Inc. 2002) software was used to perform an automated regression analysis of the tabulated MCDS estimates of RBE_{DSB} for the selected ions. Fits to the data were generated for all 3,667 built-in functions and then sorted by the quality of the fit (r^2). For normoxic cells, the empirical formula that provides the best fit to the MCDS estimates of RBE_{DSB} is

$$\text{normoxic cells}: \ \mathrm{RBE_{DSB}} = a + b - \{b^{(1-d)} + cx(d-1)\}^{\frac{1}{1-d}}, \ 2 \leqslant x \leqslant 10^5, \tag{4}$$

where $x \equiv (z_{eff}/\beta)^2$. For anoxic cells, the best-fit empirical formula is

$$\text{anoxic cells}: \ \mathrm{RBE_{DSB}} = \frac{a + \sqrt{x}\left\{c + \sqrt{x}\left[e + \sqrt{x}\left(g + i\sqrt{x}\right)\right]\right\}}{1 + \sqrt{x}\left\{b + \sqrt{x}\left[d + \sqrt{x}\left(f + h\sqrt{x}\right)\right]\right\}}, \ 2 \leqslant x \leqslant 10^5. \tag{5}$$

For aerobic and anoxic cells when $x < 2$, RBE_{DSB} approaches the asymptotic (low LET, high energy) limit 0.995 ± 0.005. In the low energy (high LET) limit ($x > 10^5$), $RBE_{DSB} = 3.41 \pm 0.01$ for normoxic cells and $RBE_{DSB} = 9.93 \pm 0.01$ for anoxic cells. Table 1 lists the fitted parameters for equations (4) and (5).

Integration of cellular dose–response functions into larger-scale MCNP simulations

To estimate the overall (average) level of DNA damage at the multi-cellular and tissue levels, Monte Carlo simulations need to correct for the effects of spatial variations in the delivered dose as well as spatial variations in the nature of the radiation field (numbers and types of particles). Formally, the dose-averaged RBE in a volume element of interest (VOI) can be computed by integrating the product $D_i(E) \cdot \mathrm{RBE}_i(E)$ over all i particle types and kinetic energies (E) and then dividing by the total absorbed dose D, i.e.

Table 1. Parameter values for empirical formulas to estimate RBE_{DSB} for normoxic and anoxic cells as a function of $(z_{eff}/\beta)^2$. The same parameter values are appropriate for electrons and light ions with $Z < 26$.

Parameter	Normoxic cells (equation (4))	Anoxic cells (equation (5))
a	0.9902	1.502
b	2.411	1.611
c	7.32×10^{-4}	1.037
d	1.539	-1.15×10^{-2}
e	—	1.35×10^{-1}
f	—	-6.096×10^{-4}
g	—	-8.230×10^{-3}
h	—	3.047×10^{-5}
i	—	3.077×10^{-4}

$$\mathrm{RBE} \equiv \frac{1}{D}\sum_i \int_0^\infty \mathrm{d}E D_i(E)\mathrm{RBE}_i(E). \tag{6}$$

From equation (6), it follows that the RBE-weighted dose computed by the product $D \times \mathrm{RBE}$ in the VOI is

$$D \cdot \mathrm{RBE} = \sum_i \int_0^\infty \mathrm{d}E D_i(E)\mathrm{RBE}_i(E). \tag{7}$$

Although equations (6) and (7) account for DNA damage arising from direct and indirect mechanisms within a VOI, DNA damage arising from extracellular signaling transmitted from one VOI to another are neglected.

MCNP has built-in tallies to record the dose from specific types of particles (e.g. F6:<pl> tallies, where <pl> denotes particle type) as well as from all particles (e.g. +F6 tally). The standard dose tallies provided by MCNP can also be modified by a user-supplied dose–response function in the form of a data table consisting of an energy-specific data entry (DE) card with the corresponding dose–response (DF) function specified on a second data entry card. RBE_{DSB} dose–response functions for selected particles (n, e^-, $^1H^+$, $^2H^+$, $^3H^+$, $^3He^{2+}$, $^4He^{2+}$, $^{12}C^{6+}$) in a format suitable for use in MCNP are available for download on the MCDS website (http://faculty.washington.edu/trawets/mcds/). For charged particle transport in MCNP, we used the default Vavilov energy straggling and the finest-allowed energy resolution in stopping powers (efac = 0.99). Except where explicitly noted otherwise, the default MCNP6 (CEM) physics models were used for neutron interactions.

Results and discussion

Trends in RBE_{DSB} as a function of $(z_{eff}/\beta)^2$

Figure 1 shows a comparison of RBE_{DSB} estimates from equations (4) and (5) to estimates obtained directly from the MCDS. The analytic formulas with the parameter estimates listed in table 1 reproduce the MCDS estimates for RBE_{DSB} within the precision of the Monte Carlo simulations (mean $\pm$ 0.01) for electrons and light ions with $Z \leqslant 26$ and $(z_{eff}/\beta)^2$ from 2 (*high energy*) to 10^5 (*low energy*). For $(z_{eff}/\beta)^2 < 2$ (low LET charged particles), the RBE_{DSB} is approximately equal to 0.995 ± 0.005 for cells irradiated under aerobic and anoxic conditions. Values of $(z_{eff}/\beta)^2$ less than unity are not meaningful because charged

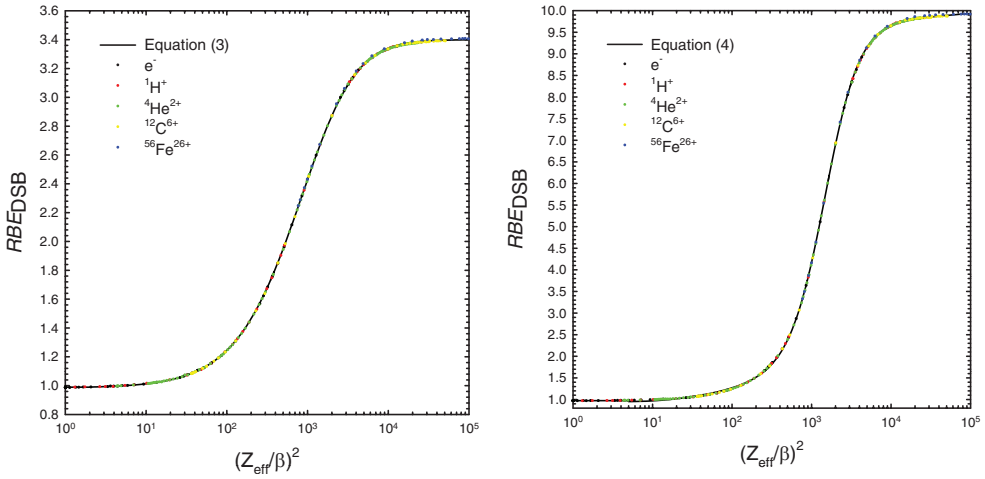

Figure 1. Estimates of RBE_{DSB} for selected ions relative to ^{60}Co γ-rays from the empirical fits (equations (3) and (4)) to estimates from MCDS simulations. Left panel: cells irradiated under normoxic conditions (8.32 DSB Gy^{-1} Gbp^{-1} for ^{60}Co). Right panel: cells irradiated under anoxic conditions (2.86 DSB Gy^{-1} Gbp^{-1} for ^{60}Co).

particles cannot exceed the speed of light in a vacuum ($\beta < 1$). In the low energy, high LET limit (i.e. $(z_{eff}/\beta)^2 > 10^4$), estimates of RBE_{DSB} approach the asymptotic values of 3.41 for normoxic cells and 9.93 for anoxic cells. As illustrated in figure 1, electrons and light ions with the same impact parameter $(z_{eff}/\beta)^2$ produce the same overall number of DSB Gy^{-1} Gbp^{-1} (or per cell). Particles with the same $(z_{eff}/\beta)^2$ produce about the same number of DSB Gy^{-1} Gbp^{-1} because DSB are primarily created in close spatial proximity (~5 nm) to the track core where numerous very low energy (high LET) δ-rays are created. The distance of 5 nm is comparable to the approximate 4 to 6 nm diffusion distance of the hydroxyl radicals usually considered responsible for the indirect action of ionizing radiation on the DNA (Roots and Okada 1975, Goodhead 1994, Nikjoo *et al* 1997, Georgakilas *et al* 2013). Although it is tempting to consider extrapolating the trends seen in figure 1 to particles with even larger values of $(z_{eff}/\beta)^2$, there is considerable uncertainty in estimates of the relative numbers of DSB induced by massive, high LET ($(z_{eff}/\beta)^2 \geqslant 10^4$) particles (e.g. figure 3 in Stewart *et al* 2011).

For large $(z_{eff}/\beta)^2$, the asymptotic trends in RBE_{DSB} apparent in figure 1 can also become inaccurate when the continuous slowing down approximation (CSDA) range of a charged particle is comparable to the dimensions of the cell nucleus (~4–6 μm). The MCDS simulates damage in small ($\leqslant$149.2 kbp) segments of DNA given a *uniform absorbed dose* of the same particle type and energy (Semenenko and Stewart 2006) or a mixture of charged particle types and energies (Stewart *et al* 2011). The estimate of the number of DNA clusters Gy^{-1} Gbp^{-1} formed in the small DNA segment is then scaled in linear fashion to the (*optional*) user-input DNA content of the cell nucleus. Therefore, the conceptual model of DNA damage induction implemented in the MCDS is most applicable to irradiation geometries in which the entire cell nucleus receives a uniform (expected or average) absorbed dose. Alternatively, the model only applies to the irradiated portion of the DNA within the nucleus that receives a uniform dose. For non-uniform irradiation, the cell nucleus needs to be sub-divided into smaller regions that receive a uniform absorbed dose. Then, damage to each uniformly irradiated sub-region can be simulated in separate runs of the MCDS. Hsiao

et al (2014) took this approach when modeling DNA damage induction from Auger-electron emitting radioisotopes distributed within the nucleus.

Relative number of DSB per particle track through the cell nucleus

The interaction of break-ends associated with two different DSB can give rise to lethal and non-lethal chromosome aberrations (Sachs *et al* 1997b, Hlatky *et al* 2002, Carlson *et al* 2008). Also, pairs of DSB in close spatial and temporal proximity are more likely to interact and form a chromosome exchange (Sachs *et al* 1997a, Carlson *et al* 2008). The DSB formed by a single ion (or the secondary charged particles produced by this ion) tend to be in closer spatial and temporal proximity than DSB formed by different (independent) light ions. Therefore, the relative numbers of DSB formed *per primary particle track* through the cell nucleus is a potentially useful, biological metric of the RBE for chromosome damage. Because DSB induction is a linear function of dose up to several hundred or thousands of Gy (Stewart *et al* 2011 and references therein), the average number of DSB Gbp^{-1} track^{-1} can be computed as the product $N_{\text{bp}}\bar{z}_{\text{F}}\Sigma_{\gamma}\text{RBE}_{\text{DSB}}$. Here, N_{bp} is the DNA content of the cell nucleus (e.g. 6 Gbp for a normal diploid human cell), $\bar{z}_F$ is the frequency-mean specific energy (in Gy), and Σ_{γ} is the number of DSB Gy^{-1} Gbp^{-1} produced by the reference radiation (e.g. ^{60}Co γ-rays). For particles with a CSDA range that is large compared to the diameter d of a target nucleus, the frequency mean specific energy is well approximated by $\bar{z}_{\text{F}} = LET/\rho d^2$ (ICRU 1983), where ρ is the mass density of the cell nucleus. When the range of the charged particle becomes comparable to the dimensions of the cell nucleus, $\bar{z}_{\text{F}}$ is usually less than $LET/\rho d^2$ because of pathlength straggling and because the stopping power is not constant as the particle passes through the cell. A very short-range particle may also lose all of its kinetic energy before passing through the nucleus. For these so-called stoppers, the frequency-mean specific energy is well approximated by $\bar{z}_{\text{F}} \cong KE/\rho d^3$, where KE is the kinetic energy of the particle incident on the cell nucleus.

The left panel of figure 2 shows the predicted trends in $\bar{z}_{\text{F}} \cdot \text{RBE}_{\text{DSB}}$ (=per track relative number of DSB) as a function of $(z_{\text{eff}}/\beta)^2$ for selected particles (e^-, $^1\text{H}^+$, $^4\text{He}^{2+}$, $^{12}\text{C}^{6+}$, ^{56}Fe).[8] The right panel of figure 2 shows an estimate of the average distance between DSB formed by an ion passing through the nucleus of a representative human cell with a cell nucleus 5 μm in diameter (horizontal dashed line in the right panel of figure 2). The average distance between DSB can be computed, under the assumption of random straight line transversals of a particle through the nucleus, by dividing the mean chord length $\bar{l}$ by the number of DSB per track $\bar{z}_{\text{F}}\text{RBE}_{\text{DSB}}\Sigma_{\gamma}N_{\text{bp}}$, i.e. $\mu\text{m per DSB} = \bar{l}/\bar{z}_{\text{F}}\text{RBE}_{\text{DSB}}\Sigma_{\gamma}N_{\text{bp}}$. The mean chord length for random particles passing through a sphere with diameter d is $2d/3$.

Although trends in RBE_{DSB} for electrons and light ions ($Z \leqslant 26$) are the same when the nucleus is uniformly irradiated (i.e. figure 1), substantial deviations in the *per track* relative number of DSB ($=\bar{z}_{\text{F}} \cdot \text{RBE}_{\text{DSB}}$) are evident as $(z_{\text{eff}}/\beta)^2$ increases. The differences in the per track number of DSB seen in the left panel of figure 2 are primarily due to the finite range of the charged particle (dotted versus solid lines), although some small effects of changes in the stopping power as the particle passes through the target can be seen in the left panel of figure 2 near the peaks in the $\bar{z}_F \cdot \text{RBE}_{\text{DSB}}$ curves. In the right panel of figure 2, the average distance between DSB formed by the same track decreases with increasing $(z_{\text{eff}}/\beta)^2$ (and LET) until

[8] The product $N_{\text{bp}}\Sigma_{\gamma}$ is independent of particle type and LET (by definition). For diploid human cells, $N_{\text{bp}}\Sigma_{\gamma} \cong 49.92$ DSB Gy^{-1} (8.32 DSB Gy^{-1} Gbp^{-1} × 6 Gbp of DNA). Therefore, the trends seen in the left panel of figure 2 are insensitive to the MCDS calculated (*absolute*) number of DSB Gy^{-1} Gbp^{-1} for ^{60}Co γ-rays (Σ_{γ}) and to the cell DNA content (N_{bp}).

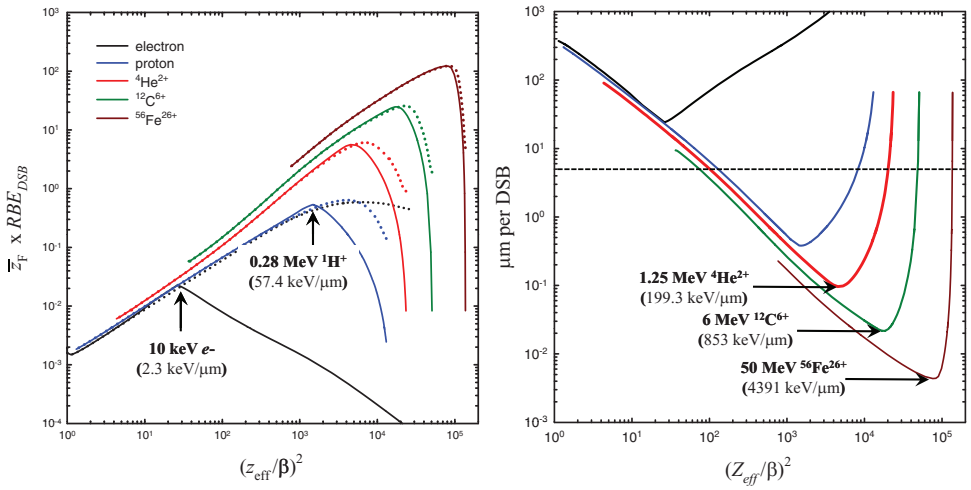

Figure 2. Left panel: Per track estimate of the number of DSB formed by selected ions relative to ^{60}Co γ-rays. Solid lines: estimates of the frequency-mean specific energy corrected for CSDA range and changes in stopping power as particles pass through a cell nucleus 5 mm in diameter (MCDS simulation). Dotted lines: frequency-mean specific energy estimated using LET/rd^2 (LET for water from the MCDS); particle type corresponds to solid line with same color. Right panel: average distance between DSB formed in the nucleus of a diploid human cell (6 Gbp of DNA) by a single charged particle. Horizontal dashed line indicates the diameter of the nucleus (5 μm). Colors and line styles indicate same particle type as left panel.

the CSDA range of the particle is approximately the same as the diameter of the cell nucleus, which is shown as a horizontal dashed line, and then increases with increasing $(z_{\text{eff}}/\beta)^2$. For electrons with kinetic energies above ~100 eV, the average distance between DSB formed by the same track is larger than a representative cell nucleus 5 μm in diameter. This observation suggests that individual electrons seldom produce more than one DSB while passing through a cell, regardless of kinetic energy. In stark contrast, protons and other light ions up to $^{56}Fe^{26+}$ have the potential to produce multiple DSB in close spatial proximity, which enhances the chance pairs of DSB will be incorrectly rejoined to form a chromosome aberration. Formation of an incomplete exchange-type chromosome aberration may also manifest in assays for DSB as an unrepairable DSB. Because DSBs formed by ionizing radiation need to be correctly repaired, or at least correctly or incorrectly rejoined, for a cell to survive, the downward trends in $\bar{z}_F \cdot \text{RBE}_{\text{DSB}}$ and the upward trend in the average distance between DSB seen in figure 2 for large $(z_{\text{eff}}/\beta)^2$ are a potential explanation for some or all of the trends in particle RBE observed in cell survival experiments (Furusawa *et al* 2000, Mehnati *et al* 2005, Czub *et al* 2008). That is, cell lethality increases with increasing $(z_{\text{eff}}/\beta)^2$ (and LET) up to a particle-specific peak (e.g. 2.3 keV μm for electrons, 57.4 keV μm^{-1} for protons, and 199.3 keV μm^{-1} for $^{4}He^{2+}$ ions) because increasing numbers of DSBs (figure 1) are created in closer and closer spatial proximity to each other (figure 2). Beyond this peak, which occurs when the CSDA range of the ion is approximately the same as the diameter of the cell nucleus, cell lethality decreases because the number of DSB Gy^{-1} Gbp^{-1} approaches an asymptotic value (figure 1) and the average distance between adjacent DSB formed by the same track increases with increasing $(z_{\text{eff}}/\beta)^2$ (figure 2). The former implies no change in cell lethality per induced DSB with increasing LET, and the latter suggests decreasing lethality per induced DSB with increasing LET. In addition to characteristic changes in the number and average distance between

adjacent DSB formed by the same track, the local complexity of the individual DSB, which tends to increase with increasing particle LET (Nikjoo *et al* 2001, Semenenko and Stewart 2004, 2006, Georgakilas *et al* 2013), are likely to have a significant impact on the regulation of alternate DSB repair pathways and on the overall kinetics and fidelity of the DSB rejoining process (Jeggo 2002, Pastwa *et al* 2003, Frankenberg-Schwager *et al* 2009, Yajima *et al* 2013, Averbeck *et al* 2014).

Photon benchmark in a representative cell culture geometry

Figure 3 shows an idealized model of a representative (generic) diagnostic x-ray machine. In the model, a mono-energetic, mono-directional beam of electrons is incident on a W target (19.25 g cm^{-3}) at an angle of 45° (figure 3, left panel). The right panel of figure 3 shows an example of a 200 and 250 kVp x-ray energy spectra with 1.5 mm and 1.3 mm of Cu filtration, respectively. To compute the RBE-weighted dose in the cell layer, we used a F6:e tally in MCNP 6.1 modified by a DE DF (RBE_{DSB}) function for electrons. As an initial test of the MCNP RBE tally, we first used the monolayer cell culture model shown in figure 3 to compute the dose-averaged RBE of ^{137}Cs γ-rays and ^{60}Co γ-rays incident. As expected, the MCNP 6.1 simulation of ^{60}Co γ-rays incident on the bottom of the cell culture dish gives an RBE_{DSB} of 1.003 ± 0.001 at the depth of maximum dose (~4.5 mm) where electronic equilibrium has been established. However for depths less than the 4.5 mm, RBE_{DSB} increases with decreasing depth to a maximum of 1.015 at a depth of 0 mm (e.g. skin surface). For ^{137}Cs γ-rays, the dose-averaged RBE_{DSB} (relative to ^{60}Co γ-rays) at the depth of maximum dose (~1.8 mm) is 1.0170 ± 0.0001 and increases with decreasing depth to 1.040 at a depth of 0 mm.

For ^{60}Co and ^{137}Cs γ-rays, the dose-averaged value of RBE_{DSB} remains constant from the depth of maximum dose (1.8 mm ^{137}Cs, 4.5 mm ^{60}Co) for depths up to at least 2 cm. For shallower depths, RBE_{DSB} may increase by 2–4% with decreasing depth. To avoid introducing systematic or seemingly random errors into dose–response measurements, experiments should be designed to expose relevant biological targets at depths beyond the depth of maximum dose in water-equivalent media, e.g. > 1.8 mm ^{137}Cs, $\geqslant 4.5$ mm ^{60}Co, $\geqslant 1.5$ cm for 6 MV x-rays, $\geqslant 2$ cm for 10 MV x-rays and $\geqslant 3.5$ cm for 18 MV x-rays. To ensure reproducibility, experiments to determine neutron RBE should also be designed with the relevant biological targets at the depth of maximum dose, which increases with increasing neutron energy.

Effects of anode material, voltage and filtration on x-ray RBE

Table 2 lists estimates of the RBE_{DSB} for cells irradiated by 60 to 250 kV x-rays under normoxic and anoxic conditions. For 200 and 250 kV x-rays with Cu filtration, the dose-averaged RBE_{DSB} in a 4 μm cell layer is 1.178 and 1.163, respectively. For 200 and 250 kV x-rays, changes in RBE_{DSB} with depth out to at least 2 cm are negligible (data not shown). As illustrated in table 2, estimates of RBE_{DSB} are far more sensitive to the amount and type of filtration than to the composition of the anode (Mo, Rh, or W) or applied voltage. For example, RBE_{DSB} for normoxic cells ranges from 1.097 for 250 kV x-rays with 1.3 mm of W filtration to a maximum of 1.240 without W filtration. For cells irradiated under anoxic conditions, RBE_{DSB} ranges from 1.157 for 250 kV x-rays with 1.3 mm of W filtration to a maximum of 1.441 without W filtration. Estimates of RBE_{DSB} are sensitive to the amount of filtration because differences in estimates of RBE_{DSB} primarily arise from the effects of secondary electrons with kinetic energies below 50 keV. That is, RBE_{DSB} increases with decreasing electron energy below ~50 keV. For electrons with kinetic energies above 50 keV, $RBE_{DSB} \cong 1$.

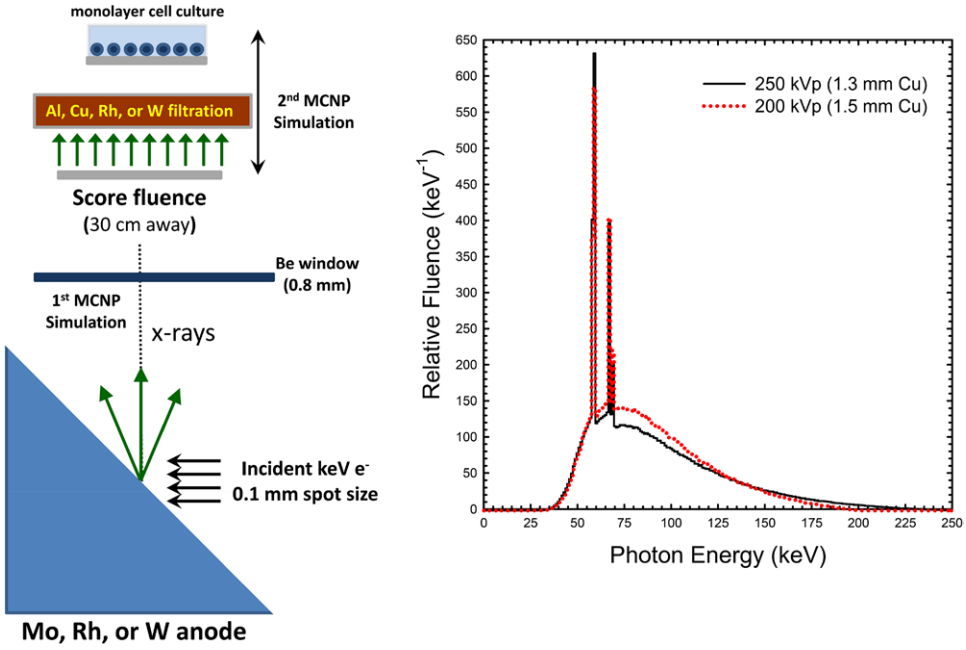

Figure 3. Left panel: model for a idealized (generic) x-ray machine with optional filtration. In the first stage of the MCNP simulation, electrons and photon are tracked down to a cutoff energy of 1 keV. A 1 keV electron and photon cutoff energy is also used in the Cu filter in the 2nd stage of the MCNP simulation. In the cell culture dish, cell layer and culture medium, electrons and photons are transported down to a cutoff energy of 100 eV. Right panel: x-ray energy spectrum from the MCNP simulation of monoenergetic 200 keV and 250 keV electrons incident on the W target with 1.5 and 1.3 mm of Cu filtration respectively.

Simulation of RBE_{DSB} effects in pristine proton pencil beams

As protons interact with tissue or other media and lose kinetic energy, proton stopping power first increases with decreasing energy and then decreases with decreasing energy for very low energy protons. Near the end of expected (average) proton range, fluence also rapidly decreases towards zero. These characteristic changes in proton fluence and stopping power give rise to the well known peak in physical dose with depth, i.e. the Bragg peak. Figure 4 shows the results of a MCNP simulation of integral depth dose (IDD) curve for a 163 MeV pencil beam normally incident upon a 40 cm × 40 cm × 40 cm water phantom. As illustrated in the left panel of figure 4, the magnitude of the Bragg peak tends to decrease as the cutoff energy for proton transport decreases. The location of the Bragg peak also shifts to slightly larger depths ($\lesssim$0.1 mm) as the cutoff energy decreases. Smaller cutoff energies substantially increase the CPU requirements of MCNP simulations but provide improved modeling of the spatial and RBE effects of high LET track ends. For cutoff energies $\leqslant$5 MeV, the choice of cutoff energy has a negligible impact on the shape of proton depth-dose (physical) curve. However as shown in the right panel of figure 4, estimates of the dose-averaged RBE_{DSB} increase with decreasing proton cutoff energies down to ~0.5 MeV. That is, the estimate of RBE_{DSB} at the Bragg peak (vertical dashed lines in figure 4) is ~1.1 for $E_{cut} = 10$ MeV, 1.14 for $E_{cut} = 5$ MeV and 1.2 for $E_{cut} \leqslant 0.5$ MeV.

Table 2. Effects of voltage, filtration and anode material on estimates of RBE_{DSB} for cells irradiated by kV x-rays under normoxic and anoxic conditions relative to ^{60}Co γ-rays. A nominal 0.8 mm of Be filtration is included in all simulations to mimic the x-ray tube window.

Voltage (kV)	Anode	Filtration	LET (keV μm^{-1})	RBE_{DSB}	
				Normoxic	Anoxic
60	W	0.8 mm Be	5.02	1.273	1.512
60	Mo	0.8 mm Be	4.74	1.253	1.472
60	Rh	0.8 mm Be	4.70	1.251	1.470
130	W	0.8 mm Be	4.80	1.259	1.483
130	Mo	0.8 mm Be	4.61	1.245	1.455
130	Rh	0.8 mm Be	4.49	1.238	1.443
200	W	0.8 mm Be + 2.5 mm Cu	3.45	1.165	1.276
200	W	0.8 mm Be + 1.5 mm Cu	3.63	1.178	1.304
200	W	0.8 mm Be + 0.5 mm Cu	3.95	1.200	1.348
200	W	0.8 mm Be	4.66	1.251	1.463
225	W	0.8 mm Be + 0.15 mm Cu	3.87	1.198	1.351
225	W	0.8 mm Be	4.52	1.241	1.444
250	W	0.8 mm Be + 1.3 mm Cu	3.39	1.163	1.278
250	W	0.8 mm Be + 1.3 mm Al	3.88	1.200	1.360
250	W	0.8 mm Be + 1.3 mm W	2.30	1.097	1.157
250	W	0.8 mm Be + 1.3 mm Rh	2.60	1.114	1.189
250	W	0.8 mm Be	4.52	1.240	1.441
250	Mo	0.8 mm Be	4.50	1.240	1.440
250	Rh	0.8 mm Be	4.31	1.230	1.420

Beyond the Bragg peak, estimates of RBE_{DSB} continue to increase with increasing depth up to about 193 $\pm$ 1 mm (~8 mm beyond the Bragg peak) and then begin to decrease. The downward trend in RBE_{DSB} beyond the Bragg peak arises because of (1) the changes in the relative numbers of low and intermediate energy primary-beam protons with depth and (2) because indirectly ionizing photons and neutrons created proximal ('upstream') to the Bragg peak subsequently create low numbers of secondary charged particles distal ('downstream') to the Bragg peak. For a monoenergetic 163 MeV pencil beam, the maximum value of the RBE_{DSB} is ~1.55. Because of energy and pathlength straggling, the peak value of RBE_{DSB} *increases* as the kinetic energy of the incident proton beam *decreases*. In general, estimates of the peak value of RBE_{DSB} are larger for monoenergetic beams than for a beam with a distribution of incident proton energies (average energy = energy of monoenergetic beam). For a nominal 163 MeV proton beam, the peak value of RBE_{DSB} decreases from 1.55 for monoenergetic protons incident on the water phantom to 1.45 for incident protons with a normal distribution ($E_{avg} = 163$) and full-width at half maximum (FWHM) of 3 MeV. As the average beam energy goes from 96 MeV to 226 MeV (FWHM = 3 MeV), the maximum value of RBE_{DSB} decreases from 1.56 ($E_{avg} = 96$ MeV) to 1.39 ($E_{avg} = 226$ MeV).

Figure 5 shows a 2D depth-dose profile for a 163 MeV proton pencil beam (5.3 mm spot size) incident on a water phantom. The bottom panel in figure 5 shows the absorbed dose profile, and the top panels illustrate the effects of cutoff energy and oxygen concentration on the size and intensity of the biological hotspot (dose $\times$ RBE_{DSB}) near the Bragg peak. The dose in all panels is normalized to the maximum physical dose for a simulation with a 1 keV proton cutoff energy. The size and intensity of the biological hotspot in the Bragg peak increases with

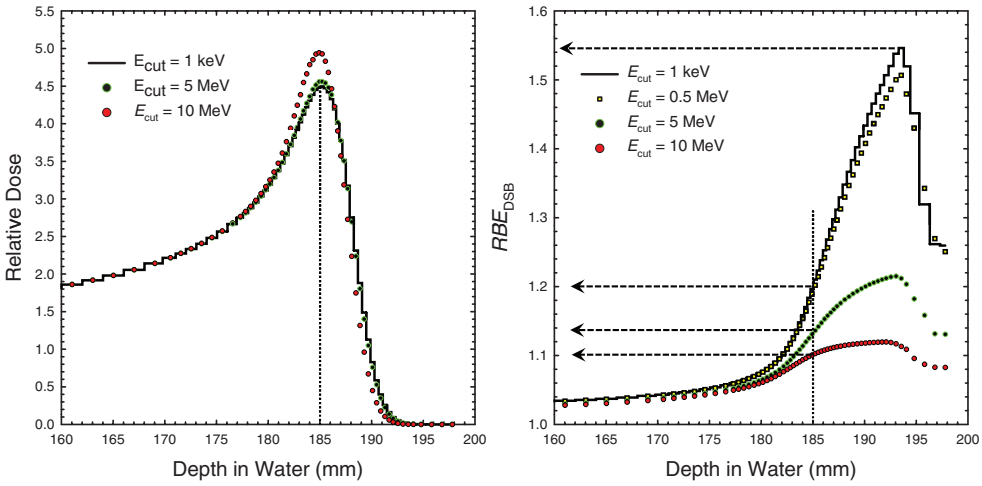

Figure 4. Effects of proton cutoff energy (E_{cut}) on MCNP simulations of a 163 MeV proton pencil beam incident on a 40 cm × 40 cm × 40 cm water phantom. Bragg peak occurs at a depth of 185 mm (*vertical dashed lines*). Left panel: absorbed dose normalized to the absorbed dose at a 2 cm depth (*not shown*). Right panel: dose-averaged RBE_{DSB}. RBE_{DSB} value at the Bragg peak (depth = 185 mm) increases from about 1.1 (E_{cut} = 10 MeV) to 1.2 (E_{cut} < 0.5 MeV). Beyond the Bragg peak, RBE_{DSB} reaches a peak value < 1.55 (E_{cut} = 1 keV).

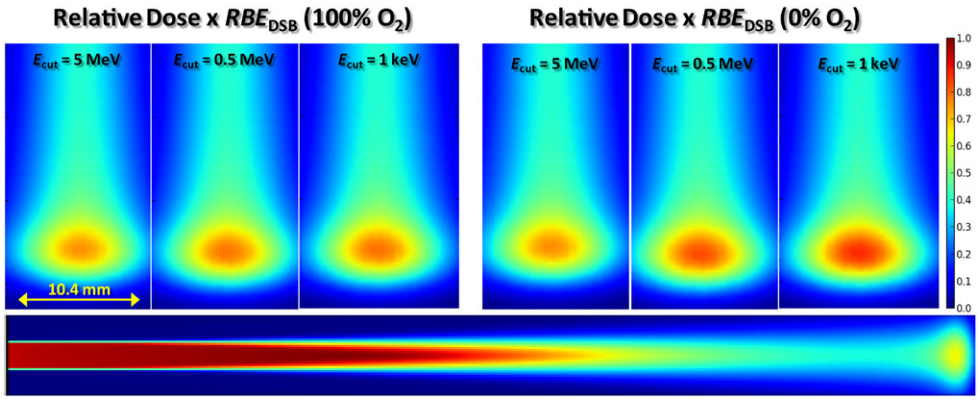

Figure 5. Effects of proton cutoff energy and oxygen level on the shape of a 163 MeV pencil (5.2 mm spot size) simulated in MCNP. Doses in all panels are normalized to the maximum physical dose for the simulation with a 1 keV proton cutoff energy and displayed using a linear color-gradient scheme. A lattice tally in MCNP was used to tally the 2D (and 3D) dose and RBE × dose distributions. Top panels: RBE_{DSB} × relative dose for well oxygenated and anoxic cells. Bottom panel: relative absorbed dose as a function of depth into water. Bragg peak occurs at a depth of ~185 mm (see also figure 4).

decreasing proton cutoff energy. Increases in the width of the biological hotspot indicate the need to account for changes in proton RBE in the lateral beam direction as well as with depth. The magnitude of the biological hotspot is also larger for cells irradiated under anoxic conditions than under normoxic conditions, which suggests proton dose painting to address hypoxia

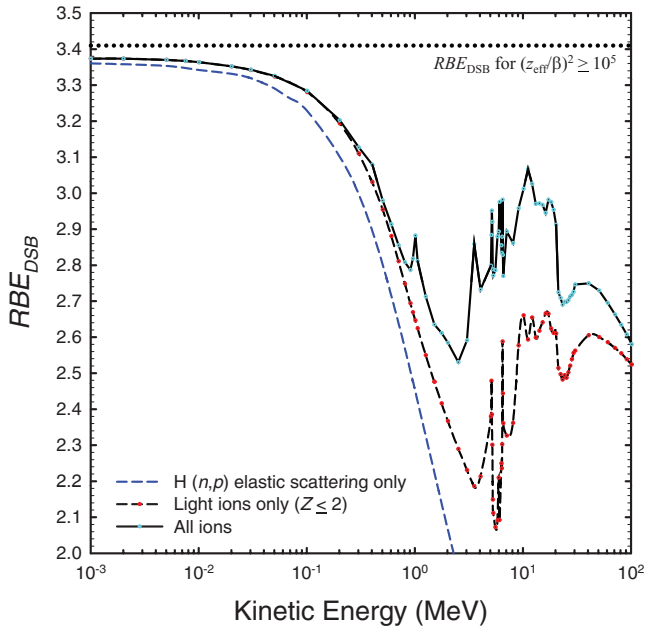

Figure 6. Estimates of RBE_{DSB} in normoxic cells irradiated by monoenergetic neutrons. Solid black line: Dose-averaged RBE for a monolayer cell culture geometry (5 cm in diameter dish surrounded by air, cell layer 10 μm thick composed of water). Neutrons and light ions ($^1H^+$, $^2H^+$, $^3H^+$, $^3He^{2+}$, and $^4He^{2+}$) are transported down to lowest allowed cutoff energy in MCNP (10^{-13} MeV for neutrons, 1 keV for light ions). Ions with $Z > 2$ have an assumed $RBE_{DSB} = 3.41$, i.e. maximum value for ions $(z_{eff}/\beta)^2 > 10^5$ (black horizontal dotted line). Dashed black lines: Dose-averaged RBE for light-ion-only simulation ($Z < 2$). Blue dashed line: dose-averaged RBE for the special case of isotropic elastic scattering of a neutron with hydrogen.

(Flynn *et al* 2008) may be more advantageous than a plan (outcome) assessment based on physical dose alone (×constant RBE = 1.1).

RBE_{DSB} for neutrons

Figure 6 shows the estimates of RBE_{DSB} for monolayer cell cultures irradiated under normoxic conditions by monoenergetic neutrons from 1 keV to 100 MeV. To estimate RBE_{DSB}, we first used the MCDS to tabulate values of RBE_{DSB} for light ions ($^1H^+$, $^2H^+$, $^3H^+$, $^3He^{2+}$, and $^4He^{2+}$) from 1 keV to 1 GeV. Then we used the standard MCNP F6 heating tally, modified by an ion-specific RBE_{DSB} dose–response function (DE DF card in MCNP), to tally RBE × dose in a 10 μm cell layer (e.g. as in the left panel of figure 3). The dose-averaged value of the RBE_{DSB} is then computed by summing $(RBE \times dose)_i$ over all i light ions ($i = {}^1H^+$, $^2H^+$, $^3H^+$, $^3He^{2+}$, and $^4He^{2+}$) and then dividing by the total dose from the same ions (dashed black line in figure 6). Neutrons and light ions were transported down to the lowest allowed energy in MCNP 6.1 (10^{-13} MeV for neutrons and 1 keV for light ions). For neutrons from 10^{-13} MeV to 20 MeV, continuous energy cross sections from ENDF/B VIII were used for H (1001.80c and 1002.80c) and O (8016.80c and 8017.80c). From 20 to 100 MeV, we used the default (CEM) MCNP6 neutron physics models for interactions with ^2H and ^{17}O, and the ENDF/B VI continuous energy cross section library for ^1H (1001.66c), and the ENDF/B VIII cross sections for

Table 3. Estimates of RBE_{DSB} for monolayer cell cultures irradiated in air by selected fission neutron sources (appendix H MCNP manual) and the University of Washington Clinical Neutron Therapy System (CNTS). The UW CNTS neutron energy spectrum (50.5 MeV $^{1}H^{+}$ incident on Be target) have an average energy of about 20 MeV. The PuBe and D_2O moderated ^{252}Cf neutron spectra are taken from Anderson *et al* (1963) and ISO Standard 8529 (1989), respectively.

	Fraction of dose		Neutron RBE_{DSB}		
Source	Light ions	Heavy ions	Light ions only	All ions[a]	Max[b]
PuBe	0.65	0.35	2.49	2.63	2.82
^{252}Cf	0.77	0.23	2.60	2.66	2.78
CNTS	0.75	0.25	2.61	2.67	2.80
^{242}Cm	0.78	0.22	2.61	2.67	2.78
^{244}Cm	0.78	0.22	2.61	2.67	2.78
^{239}Pu	0.78	0.22	2.62	2.67	2.79
^{232}Th	0.78	0.22	2.62	2.67	2.79
^{240}Pu	0.79	0.21	2.62	2.67	2.79
^{233}U	0.79	0.21	2.62	2.68	2.79
^{238}U	0.79	0.21	2.63	2.68	2.79
^{235}U	0.79	0.21	2.63	2.68	2.79
D_2O moderated ^{252}Cf	0.85	0.15	2.91	2.90	2.98

[a] Contribution of ions with $Z > 2$ estimated using $RBE_{DSB} = 2.875$ (50 MeV $^{12}C^{6+}$ ion with $(z_{eff}/\beta)^2 = 3825$).
[b] Contribution of ions with $Z > 2$ estimated using asymptotic RBE_{DSB} of 3.41 for $(z_{eff}/\beta)^2 = 10^5$ (horizontal dotted line in figure 6).

^{16}O (1001.80c). Because ions with kinetic energies less than 100 MeV and $Z > 2$ have a large $(z_{eff}/\beta)^2$, the contributions to the overall neutron RBE of more massive ions ($Z > 2$) were estimated by multiplying the dose deposited in the cell layer by these ions by the maximum $RBE_{DSB} = 3.41$ (horizontal dotted line in figure 6). For each energy, simulations are based on 10^9 source neutrons passing through the cell culture dish.

For comparison to the estimates of RBE_{DSB} from the MCNP simulations, we also estimated RBE_{DSB} for the special case when neutrons only interact with ^{1}H through an isotropic (n, p) elastic scattering mechanism (figure 6, blue dashed line). For this special case, the distribution of secondary proton energies produced by neutron elastic scattering is well approximated by a uniform probability distribution with a mean equal to ½ the kinetic energy of the incident neutron (Caswell 1966). As illustrated in figure 6, (n, p) elastic scattering with H is the dominant neutron interaction mechanism in water between about 1 keV and 1 MeV. Below a few hundred keV, the neutron RBE for DSB induction approaches the asymptotic, high $(z_{eff}/\beta)^2$ limit, of $RBE_{DSB} = 3.41$ (dotted horizontal line in figure 6). Above about 4 MeV, (n, α) and other nuclear reactions, many of which have resonances in the cross sections up to about 30 MeV, have a significant impact on the estimates of neutron RBE.

Table 3 lists dose-averaged estimates of RBE_{DSB} for selected neutron fission spectra and for the fast neutron Clinical Neutron Therapy System (CNTS) at the University of Washington (Stelzer *et al* 1994, Kalet *et al* 2013). For fission neutrons without additional moderation, as well as the higher energy CNTS neutron energy spectrum, 65% to 80% of the dose deposited in cell layer (composed of water) is from light ions ($Z \leqslant 2$) and the remainder is (primarily) from recoil $^{16}N^{7+}$ and $^{12}C^{6+}$ ions. A 100 MeV $^{12}C^{6+}$ ion has a $(z_{eff}/\beta)^2 = 2012$ and $RBE_{DSB} = 2.875$, and a 50 MeV $^{12}C^{6+}$ ion has a $(z_{eff}/\beta)^2 = 3825$ and $RBE_{DSB} = 3.158$. Recoil $^{16}N^{7+}$ ions have larger values of $(z_{eff}/\beta)^2$ and RBE_{DSB} than $^{12}C^{6+}$ ions with the same

(corresponding) kinetic energy. As illustrated in table 3, estimates of RBE_{DSB} for fission, moderated fission, PuBe and the CNTS neutrons differ by 3–7% depending on the method used to account for the effects of ions with $Z > 2$. However as a first approximation, the data reported in table 3 suggest that an $RBE_{DSB} = 2.7 \pm 0.1$ is appropriate for fission neutrons, CNTS neutrons and PuBe neutrons. For ^{252}Cf neutrons moderated by 30 cm of heavy water, a slightly higher RBE_{DSB} of 2.95 ± 0.05 is more appropriate.

Summary and conclusions

We have developed an efficient computational strategy to incorporate important characteristics of charge particle tracks at the molecular and sub-cellular level into larger-scale Monte Carlo dosimetry models more relevant to laboratory experiments and, ultimately, to radiation oncology and radiation protection. Our approach propagates information across relevant physical and biological scales by integrating information from an independently tested, small-scale biophysical model (i.e. the MCDS) with a larger-scale, general purpose, Monte Carlo radiation transport model (MCNP). Because our approach is computationally efficient, a virtuous (positive) feedback loop can be created to accelerate future refinement and testing of improved RBE models. That is, independent testing of the MCDS and MCNP can be supplemented by *additional testing* of a combined (multiscale) model that better mimics the details of specific *in vitro* or *in vivo* experiments. As an added benefit, the encapsulation within separate models of the physics and biology at different spatial scales helps minimize the use of extraneous (challenging to measure or predict from first principles) parameters. For example, the combined MCDS + MCNP approach developed in this work does not require the specification of any purely *ad hoc* (empirical) parameters to estimate the RBE for initial DSB formation at the cellular, multi-cellular or tissue levels.

Efforts to develop computationally efficient strategies to connect physics (dosimetry) and chemistry at the molecular and cellular levels to radiobiological effects on the larger tumor and tissue levels are crucial for ongoing efforts to fully exploit the therapeutic potential of light ions for the treatment of cancer. In 2010, Mairani *et al* (2010) combined the FLUKA Monte Carlo code system with the local effect model (LEM) to determine dose-averaged RBE values for therapeutic carbon ions (endpoint of reproductive cell death). Similarly, the MCDS in combination with the repair–misrepair-fixation (RMF) cell survival model (Carlson *et al* 2008) has been used in combination with analytic dosimetry models (Carlson *et al* 2008, Frese *et al* 2012) and Monte Carlo simulations (Polster *et al* 2015, Kamp *et al* 2015) to determine dose-averaged RBE values for light ions. Estimates of the RBE for light ions have also been determined from Geant4 simulations in combination with the cell-level microdosimetric-kinetic model (MKM) model (Hawkins 2003, 1998, 2009) for reproductive cell death (Remmes *et al* 2012, Burigo *et al* 2015). Simulations such as these represent the current state-of-the-art with regards to propagating the biophysical effects of light ion tracks from the subcellular level to RBE models for tumor targets and tissues.

For biological endpoints in which DSB are an important initiating event, such as the formation of chromosome aberrations and reproductive cell death (Cornforth and Bedford 1987, Bedford 1991, Sachs *et al* 1997b, Hlatky *et al* 2002, Carlson *et al* 2008, Stewart *et al* 2011), the results shown in figures 1 and 2 suggest that any experimentally observed differences in the RBE of particles with the same $(z_{eff}/\beta)^2$ are more likely to be due to the *per track* number of DSB and/or proximity effects (Sachs *et al* 1997a, Hlatky *et al* 2002) than to differences in the overall number of DSB *per unit dose* (figure 1). The effects of local DSB complexity also play a role in the overall kinetics and fidelity of the DSB rejoining process (Jeggo

2002, Pastwa *et al* 2003, Frankenberg-Schwager *et al* 2009, Yajima *et al* 2013, Averbeck *et al* 2014). The formation of unrepairable DSB and/or the biological processing of repairable DSB into lethal chromosome aberrations provides a conceptually appealing and plausible basis for trends in the RBE for reproductive cell death as a function of particle type, LET and oxygen concentration. The induction and biological processing of DSBs, which are sometimes referred to as sublethal or potentially lethal damage (Bedford 1991), are a common aspect of mechanistic models for the effects of particle LET on reproductive cell death, including the MKM (Hawkins 2003, 1998, 2009), recent versions of the LEM (Friedrich *et al* 2012a, 2012b, Tommasino *et al* 2013, 2015) and the RMF model (Carlson *et al* 2008, Frese *et al* 2012). The MKM and RMF models also have close conceptual and mathematical roots in the even earlier repair–misrepair (RMR) model of Tobias (1985) and the lethal and potentially lethal (LPL) model of Curtis (1986).

A conceptual difference between the RMF (and RMR and LPL) models and the LEM and MKM is that the former considers the entire cell nucleus as the domain for DSB interactions whereas the LEM and MKM models treat the interactions and consequences of DSB (sublethal or potentially lethal damage) within the same sub-cellular domain (e.g. a chromatin loop) different from DSB interactions among adjacent or nearby domains. In the RMF model, trends in the RBE for reproductive cell death with particle type, LET and oxygen concentration primarily arise from changes in (1) the number of DSB Gy^{-1} Gbp^{-1} (figure 1) and (2) the number of DSB $track^{-1}$ Gbp^{-1} (figure 2). The former relates to the overall level of damage sustained by a cell (total number of repair events) and the latter relates to the impact of other nearby DSB (i.e. proximity effects) on the kinetics and accuracy of the DSB rejoining process. In the RMF model, the overall rates and fidelity of the DSB rejoining process are cell, tumor and tissue-specific, but the *relative* numbers and sub-cellular spatial distribution of DSB are considered independent of cell, tumor and tissue type, i.e. RBE_{DSB} and $\bar{z}_F RBE_{DSB}$ are about the same for all mammalian cells but vary dramatically with particle type, LET and oxygen concentration (figures 1 and 2).

In the RMF model, the cell, tumor and tissue-specific aspects of the biological processing of DSB (kinetics and fidelity of DSB repair) are embedded in two adjustable parameters that are cell- and tissue-specific but independent of particle type and LET. The overall numbers of DSB as well as effects of nearby DSB ('proximity effects') are modeled in the RMF by distinguishing between intra-track and inter-track DSB interaction mechanisms. The LEM and MKM models also treat, in effect, the biological processing of sublethal or potentially lethal DSB into lethal damage as a cell, tumor or tissue specific process. However, the use of subcellular interaction domains in the LEM and MKM models introduces at least one additional parameter into the modeling process (size of the domain *and* cell nucleus) compared to use of a single domain (size of the cell nucleus) in the RMF, LPL, and RMR models. Although the LEM and MKM approach has merit, it remains an open question as to whether the added flexibility of the LEM and MKM suffice to justify introducing an additional free parameter into the RBE modeling process compared to the LPL, RMR and RMF models.

Larger scale simulations of particle RBE also provide useful information about the potential biological equivalence of commonly used (low LET) reference radiations, such as ^{60}Co γ-rays, ^{137}Cs γ-rays and kV or MV x-rays. For example, does the choice of voltage, anode material, and the amount of filtration have an impact on the RBE characteristics of x-rays sources? The results shown in table 2 indicate that the amount and type of filtration is the most important determinant of low energy (60–250 kV) x-ray RBE. One might also ask whether or not it is likely that RBE estimates for a monolayer cell culture will differ when cells are irradiated from above rather than below? Or, does the amount of medium, thickness of the dish or presence of backscatter or other materials above or below the cell layer (*region of interest*)

matter in experimental determinations of particle RBE? As explained below, experimental details such as these may sometimes have a significant impact on experimental determinations of particle RBE.

For simulations in which the cell layer is at an effective depth less than the depth of maximum dose (i.e. before charged particle equilibrium has been established), we found that RBE_{DSB} estimates varied by up to 1.5% for ^{60}Co γ-rays and by up to 4% for ^{137}Cs γ-rays. Beyond the depth of maximum dose (~1.8 mm for ^{137}Cs and 4.5 mm for ^{60}Co), the RBE_{DSB} for ^{60}Co γ-rays remained constant (~1.00) out to depths of at least 2.0 cm. For ^{137}Cs γ-rays, our simulations indicate an $RBE_{DSB} \cong 1.017$ (relative to ^{60}Co γ-rays at depths > 4.5 mm) from 1.8 mm to 2.0 cm. Considerations of charge particle equilibrium and the depth of maximum dose are also relevant to the determination of neutron RBE. For example, fast neutrons from the UW CNTS (~20 MeV average energy) have a depth of maximum dose in water of about 1.7 cm. For shallower depths, it is primarily the buildup of protons rather than electrons that determines the depth of maximum dose. For neutrons in water with kinetic energies less than about 1–2 MeV, estimates of RBE_{DSB} are largely determined by the energy distribution of secondary protons produced in elastic (n, p) interactions with hydrogen (figure 6 solid and blue dashed lines). In the buildup region, low energy (higher LET) protons reach equilibrium at shallower depths than higher energy (lower LET) protons. Therefore, estimates of neutron RBE_{DSB} at depths less than 1.7 cm (e.g. near surface of a patient's skin) may be closer to the maximum RBE of 3.41 (dotted line in figure 6) than to the estimates of 2.7 ± 0.1 reported in table 3. In soft tissue and bone, the elemental composition of the intra- and extracellular environment alters the estimates of RBE_{DSB} as the relative doses from light and heavy ions changes with the elemental composition of fat, soft tissue and bone. Explicit multiscale simulations that incorporate the larger scale extracellular and tissue environment into RBE modeling at the sub-cellular level are needed to address these issues in a precise and quantitative way.

For 60 to 250 kV x-rays, we found that the composition of the anode and the voltage both have a small (<1%) effect on estimates of RBE_{DSB}. However, estimates of RBE_{DSB} ranged from about 1.1 to 1.25 depending on the amount and type of filtration (table 2); for anoxic cells, estimates of RBE_{DSB} for low energy x-rays (relative to ^{60}Co γ-rays) may be as large as 1.5. Insufficient information to fully correct for the RBE characteristics of the low LET reference radiation may be a significant source of uncertainty in the determination of proton RBE within pristine and spread out Bragg peaks (SOBP). For example, numerous instances of a proton RBE less than unity were reported in a careful meta-analysis of published proton RBE experiments (Paganetti 2014). Inter-laboratory differences in the absolute calibration and RBE characteristics of the reference radiation are a plausible explanation for reports of proton RBE values < 1. To achieve, for example, a proton RBE of 1.0 ± 0.05 (95% confidence interval) requires absolute dosimetry for the proton beam *and* reference radiation of $\pm 1.8\%$. Also, an RBE_{DSB} of 1.1 relative to ^{60}Co γ-rays could be reported as an RBE_{DSB} estimate of 0.88 relative to unfiltered (or lightly filtered) 60–250 kV x-rays (table 2).

Based on our experiences with coupled (multiscale) MCNP + MCDS simulations of initial DSB formation by photons, neutron and light ions, we offer the following recommendations to aid in the design, interpretation and intercomparison of future particle RBE experiments:

(1) To the extent possible, design *in vitro* and *in vivo* experiments in ways that establish charge particle equilibrium at the location of the RBE measurement. Considerations of particle equilibrium apply to the reference radiation and to beams of neutral or charged particles. When low energy x-rays are used as the reference radiation, report at a minimum (*a*) the amount and type of filtration and (*b*) the applied voltage, especially if less than about

60 kV. The composition of the anode does not appear critical based on our Monte Carlo simulations (table 2), although it may still be worth reporting.

(2) Report the absolute calibration of laboratory-specific reference radiation sources relative to a low LET source maintained by an independent Accredited Dosimetry Calibration Laboratory (ADCL). Determinations of particle RBE are sensitive to the absolute calibration of the selected reference radiation as well as to the RBE of the reference radiation relative to (for example) ^{60}Co γ-rays.

(3) For the characterization of incident beams of charged particles, report the RBE of the particle in the high energy (low LET) plateau region of the Bragg peak (e.g. depths < 160 mm in figure 4) relative to the reference radiation of ultimate interest (e.g. MV x-rays or ^{60}Co γ-rays). Then report the particle RBE at other locations proximal, distal and lateral to the particle beam calibration point (in plateau region). This approach will enable the clean separation of the RBE and dosimetric uncertainties associated with the choice of reference radiation (recommendation #1 and 2) from spatial variations in particle RBE at different locations within the particle beam.

(4) Conduct Monte Carlo simulations to aid in the design and interpretation of specific laboratory experiments. Such simulations can help correct for differences in laboratory and experiment-specific irradiation techniques and serve as an additional test of alternate and refined multiscale biophysical models. Future work in this area should include *in vitro* and *in vivo* modeling and measurements of the RBE for biological endpoints relevant to mutagenesis, carcinogenesis and the biological optimization of proton and carbon ion therapy (e.g. spatial variations in proton and carbon ion RBE). Relevant endpoints include, but are not limited to, other categories of initial DNA damage (complex DSB, individual and complex clusters of individual strand breaks and base damage that do not constitute a DSB), chromosome aberrations and reproductive cell death. Additional studies are needed to test the hypothesis that the RBE for DSB induction, and other related molecular or cellular endpoints, are useful as computational surrogates for the optimization of clinical outcomes (local tumor control and normal tissue damage) in hadron therapy.

Acknowledgments

Research supported in part by funding received by one of us (GM) from the US Department of Energy (DOE) Integrated University Program.

Conflict of interest

None.

References

Alloni D, Campa A, Belli M, Esposito G, Facoetti A, Friedland W, Liotta M, Mariotti L, Paretzke H G and Ottolenghi A 2010 A Monte Carlo study of the radiation quality dependence of DNA fragmentation spectra *Radiat. Res.* **173** 263–71

Alloni D, Campa A, Friedland W, Mariotti L and Ottolenghi A 2013 Integration of Monte Carlo simulations with PFGE experimental data yields constant RBE of 2.3 for DNA double-strand break induction by nitrogen ions between 125 and 225 keV/mum LET *Radiat. Res.* **179** 690–7

Anderson M E and Bond W H 1963 Neutron spectrum of a plutonium–beryllium source *Nucl. Phys.* **43** 330–8

Averbeck N B, Ringel O, Herrlitz M, Jakob B, Durante M and Taucher-Scholz G 2014 DNA end resection is needed for the repair of complex lesions in G1-phase human cells *Cell Cycle* **13** 2509–16

Ballarini F, Biaggi M, Merzagora M, Ottolenghi A, Dingfelder M, Friedland W, Jacob P and Paretzke H G 2000 Stochastic aspects and uncertainties in the prechemical and chemical stages of electron tracks in liquid water: a quantitative analysis based on Monte Carlo simulations *Radiat. Environ. Biophys.* **39** 179–88

Barkas W H and Evans D A 1963 *Nuclear Research Emulsions* (New York: Academic)

Bedford J S 1991 Sublethal damage, potentially lethal damage, and chromosomal aberrations in mammalian cells exposed to ionizing radiations *Int. J. Radiat. Oncol. Biol. Phys.* **21** 1457–69

Bernal M A, deAlmeida C E, Sampaio C, Incerti S, Champion C and Nieminen P 2011 The invariance of the total direct DNA strand break yield *Med. Phys.* **38** 4147–53

Bernhardt P, Friedland W, Meckbach R, Jacob P and Paretzke H G 2002 Monte Carlo simulation of DNA damage by low LET radiation using inhomogeneous higher order DNA targets *Radiat. Prot. Dosim.* **99** 203–6

Burigo L, Pshenichnov I, Mishustin I and Bleicher M 2015 Comparative study of dose distributions and cell survival fractions for 1H, 4He, 12C and 16O beams using Geant4 and Microdosimetric Kinetic model *Phys. Med. Biol.* **60** 3313–31

Byrne M, Wray J, Reinert B, Wu Y, Nickoloff J, Lee S H, Hromas R and Williamson E 2014 Mechanisms of oncogenic chromosomal translocations *Ann. NY Acad. Sci.* **1310** 89–97

Campa A *et al* 2005 DNA DSB induced in human cells by charged particles and gamma rays: experimental results and theoretical approaches *Int. J. Radiat. Biol.* **81** 841–54

Campa A *et al* 2009 DNA fragmentation induced in human fibroblasts by 56Fe ions: experimental data and Monte Carlo simulations *Radiat. Res.* **171** 438–45

Carlson D J, Stewart R D, Semenenko V A and Sandison G A 2008 Combined use of Monte Carlo DNA damage simulations and deterministic repair models to examine putative mechanisms of cell killing *Radiat. Res.* **169** 447–59

Caswell R S 1966 Deposition of energy by neutrons in spherical cavities *Radiat. Res.* **27** 92–107

Cornforth M N and Bedford J S 1987 A quantitative comparison of potentially lethal damage repair and the rejoining of interphase chromosome breaks in low passage normal human fibroblasts *Radiat. Res.* **111** 385–405

Curtis S B 1986 Lethal and potentially lethal lesions induced by radiation—a unified repair model *Radiat. Res.* **106** 252–70

Czub J *et al* 2008 Biological effectiveness of (12)C and (20)Ne ions with very high LET *Int. J. Radiat. Biol.* **84** 821–9

Ezzati A O, Xiao Y, Sohrabpour M and Studenski M T 2015 The effect of energy spectrum change on DNA damage in and out of field in 10 MV clinical photon beams *Med. Biol. Eng. Comput.* **53** 67–75

Flynn R T, Bowen S R, Bentzen S M, Rockwell Mackie T and Jeraj R 2008 Intensity-modulated x-ray (IMXT) versus proton (IMPT) therapy for theragnostic hypoxia-based dose painting *Phys. Med. Biol.* **53** 4153–67

Frankenberg-Schwager M, Gebauer A, Koppe C, Wolf H, Pralle E and Frankenberg D 2009 Single-strand annealing, conservative homologous recombination, nonhomologous DNA end joining, and the cell cycle-dependent repair of DNA double-strand breaks induced by sparsely or densely ionizing radiation *Radiat. Res.* **171** 265–73

Frese M C, Yu V K, Stewart R D and Carlson D J 2012 A mechanism-based approach to predict the relative biological effectiveness of protons and carbon ions in radiation therapy *Int. J. Radiat. Oncol. Biol. Phys.* **83** 442–50

Friedland W, Bernhardt P, Jacob P, Paretzke H G and Dingfelder M 2002 Simulation of DNA damage after proton and low LET irradiation *Radiat. Prot. Dosim.* **99** 99–102

Friedland W, Dingfelder M, Jacob P and Paretzke H G 2005 Calculated DNA double-strand break and fragmentation yields after irradiation with He ions *Radiat. Phys. Chem.* **72** 279–86

Friedland W, Jacob P, Bernhardt P, Paretzke H G and Dingfelder M 2003 Simulation of DNA damage after proton irradiation *Radiat. Res.* **159** 401–10

Friedrich T, Durante M and Scholz M 2012a Modeling cell survival after photon irradiation based on double-strand break clustering in megabase pair chromatin loops *Radiat. Res.* **178** 385–94

Friedrich T, Scholz U, Elsasser T, Durante M and Scholz M 2012b Calculation of the biological effects of ion beams based on the microscopic spatial damage distribution pattern *Int. J. Radiat. Biol.* **88** 103–7

Furusawa Y, Fukutsu K, Aoki M, Itsukaichi H, Eguchi-Kasai K, Ohara H, Yatagai F, Kanai T and Ando K 2000 Inactivation of aerobic and hypoxic cells from three different cell lines by accelerated (3)He-, (12)C- and (20)Ne-ion beams *Radiat. Res.* **154** 485–96

Georgakilas A G, O'Neill P and Stewart R D 2013 Induction and repair of clustered DNA lesions: what do we know so far? *Radiat. Res.* **180** 100–9

Goodhead D T 1994 Initial events in the cellular effects of ionizing radiations: clustered damage in DNA *Int. J. Radiat. Biol.* **65** 7–17

Goorley J T *et al* 2013 Initial MCNP6 release overview—MCNP6 version 1.0 *LA-UR*-13-22934 (http://laws.lanl.gov/vhosts/mcnp.lanl.gov/pdf_files/la-ur-13-22934.pdf)

Hawkins R B 1998 A microdosimetric-kinetic theory of the dependence of the RBE for cell death on LET *Med. Phys.* **25** 1157–70

Hawkins R B 2003 A microdosimetric-kinetic model for the effect of non-Poisson distribution of lethal lesions on the variation of RBE with LET *Radiat. Res.* **160** 61–9

Hawkins R B 2009 The relationship between the sensitivity of cells to high-energy photons and the RBE of particle radiation used in radiotherapy *Radiat. Res.* **172** 761–76

Hlatky L, Sachs R K, Vazquez M and Cornforth M N 2002 Radiation-induced chromosome aberrations: insights gained from biophysical modeling *Bioessays* **24** 714–23

Holley W R and Chatterjee A 1996 Clusters of DNA induced by ionizing radiation: formation of short DNA fragments: I. Theoretical modeling *Radiat. Res.* **145** 188–99

Hsiao Y Y, Hung T H, Tu S J and Tung C J 2014 Fast Monte Carlo simulation of DNA damage induction by Auger-electron emission *Int. J. Radiat. Biol.* **90** 392–400

Hsiao Y and Stewart R D 2008 Monte Carlo simulation of DNA damage induction by x-rays and selected radioisotopes *Phys. Med. Biol.* **53** 233–44

ICRU 1983 *Microdosimetry* (Bethesda: International Commission of Radiation Units and Measurements)

International Organization for Standardization 1989 Neutron Reference Radiations for Calibrating As a Function of Neutron Energy, International Standard ISO-8529

Jeggo P A 2002 The fidelity of repair of radiation damage *Radiat. Prot. Dosim.* **99** 117–22

Kalet A M, Sandison G A, Phillips M H and Parvathaneni U 2013 Validation of the Pinnacle(3) photon convolution-superposition algorithm applied to fast neutron beams *J. Appl. Clin. Med. Phys.* **14** 4305

Kamp F C G, Mairani A, Parodi K, Wilkens J J and Carlson D J 2015 Fast biological modeling for voxel-based heavy ion therapy treatment planning using the mechanistic repair-misrepair-fixation (RMF) model and nuclear fragment spectra *Int. J. Radiat. Oncol. Biol. Phys.* **93** 557–68

Kirkby C, Ghasroddashti E, Poirier Y, Tambasco M and Stewart R D 2013 RBE of kV CBCT radiation determined by Monte Carlo DNA damage simulations *Phys. Med. Biol.* **58** 5693–704

Kreipl M S, Friedland W and Paretzke H G 2009 Interaction of ion tracks in spatial and temporal proximity *Radiat. Environ. Biophys.* **48** 349–59

Mairani A, Brons S, Cerutti F, Fasso A, Ferrari A, Kramer M, Parodi K, Scholz M and Sommerer F 2010 The FLUKA Monte Carlo code coupled with the local effect model for biological calculations in carbon ion therapy *Phys. Med. Biol.* **55** 4273–89

Mehnati P, Morimoto S, Yatagai F, Furusawa Y, Kobayashi Y, Wada S, Kanai T, Hanaoka F and Sasaki H 2005 Exploration of 'over kill effect' of high-LET Ar- and Fe-ions by evaluating the fraction of non-hit cell and interphase death *J. Radiat. Res.* **46** 343–50

Morgan W F 2003a Non-targeted and delayed effects of exposure to ionizing radiation: I. Radiation-induced genomic instability and bystander effects *in vitro Radiat. Res.* **159** 567–80

Morgan W F 2003b Non-targeted and delayed effects of exposure to ionizing radiation: II. Radiation-induced genomic instability and bystander effects *in vivo*, clastogenic factors and transgenerational effects *Radiat. Res.* **159** 581–96

Mothersill C and Seymour C B 1998 Mechanisms and implications of genomic instability and other delayed effects of ionizing radiation exposure *Mutagenesis* **13** 421–6

Neshasteh-Riz A, Koosha F, Mohsenifar A and Mahdavi S R 2012 DNA damage induced in glioblastoma cells by I-131: a comparison between experimental data and Monte Carlo simulation *Cell J.* **14** 25–30 (PMC: 3635817)

Nikjoo H, Bolton C E, Watanabe R, Terrissol M, O'Neill P and Goodhead D T 2002 Modelling of DNA damage induced by energetic electrons (100 eV to 100 keV) *Radiat. Prot. Dosim.* **99** 77–80

Nikjoo H, O'Neill P, Goodhead D T and Terrissol M 1997 Computational modelling of low-energy electron-induced DNA damage by early physical and chemical events *Int. J. Radiat. Biol.* **71** 467–83
Nikjoo H, O'Neill P, Terrissol M and Goodhead D T 1994 Modelling of radiation-induced DNA damage: the early physical and chemical event *Int. J. Radiat. Biol.* **66** 453–7
Nikjoo H, O'Neill P, Terrissol M and Goodhead D T 1999 Quantitative modelling of DNA damage using Monte Carlo track structure method *Radiat. Environ. Biophys.* **38** 31–8
Nikjoo H, O'Neill P, Wilson W E and Goodhead D T 2001 Computational approach for determining the spectrum of DNA damage induced by ionizing radiation *Radiat. Res.* **156** 577–83
Obe G, Pfeiffer P, Savage J R, Johannes C, Goedecke W, Jeppesen P, Natarajan A T, Martinez-Lopez W, Folle G A and Drets M E 2002 Chromosomal aberrations: formation, identification and distribution *Mutat. Res.* **504** 17–36
Paganetti H 2014 Relative biological effectiveness (RBE) values for proton beam therapy. Variations as a function of biological endpoint, dose, and linear energy transfer *Phys. Med. Biol.* **59** R419–72
Pastwa E, Neumann R D, Mezhevaya K and Winters T A 2003 Repair of radiation-induced DNA double-strand breaks is dependent upon radiation quality and the structural complexity of double-strand breaks *Radiat. Res.* **159** 251–61
Pater P, Seuntjens J, El Naqa I and Bernal M A 2014 On the consistency of Monte Carlo track structure DNA damage simulations *Med. Phys.* **41** 121708
Polster L *et al* 2015 Extension of TOPAS for the simulation of proton radiation effects considering molecular and cellular endpoints *Phys. Med. Biol.* **60** 5053–70
Remmes N B, Herman M G and Kruse J J 2012 Optimizing normal tissue sparing in ion therapy using calculated isoeffective dose for ion selection *Int. J. Radiat. Oncol. Biol. Phys.* **83** 756–62
Reniers B, Liu D, Rusch T and Verhaegen F 2008 Calculation of relative biological effectiveness of a low-energy electronic brachytherapy source *Phys. Med. Biol.* **53** 7125–35
Roots R and Okada S 1975 Estimation of life times and diffusion distances of radicals involved in x-ray-induced DNA strand breaks of killing of mammalian cells *Radiat. Res.* **64** 306–20
Rothkamm K and Lobrich M 2002 Misrepair of radiation-induced DNA double-strand breaks and its relevance for tumorigenesis and cancer treatment (review) *Int. J. Oncol.* **21** 433–40 (PMID: 12118342)
Sachs R K, Chen A M and Brenner D J 1997a Review: proximity effects in the production of chromosome aberrations by ionizing radiation *Int. J. Radiat. Biol.* **71** 1–19
Sachs R K, Hahnfeld P and Brenner D J 1997b The link between low-LET dose–response relations and the underlying kinetics of damage production/repair/misrepair *Int. J. Radiat. Biol.* **72** 351–74
Semenenko V A and Stewart R D 2004 A fast Monte Carlo algorithm to simulate the spectrum of DNA damages formed by ionizing radiation *Radiat. Res.* **161** 451–7
Semenenko V A and Stewart R D 2005 Monte Carlo simulation of base and nucleotide excision repair of clustered DNA damage sites. II. Comparisons of model predictions to measured data *Radiat. Res.* **164** 194–201
Semenenko V A and Stewart R D 2006 Fast Monte Carlo simulation of DNA damage formed by electrons and light ions *Phys. Med. Biol.* **51** 1693–706
Semenenko V A, Stewart R D and Ackerman E J 2005 Monte Carlo simulation of base and nucleotide excision repair of clustered DNA damage sites: I. Model properties and predicted trends *Radiat. Res.* **164** 180–93
Stelzer K J, Laramore G E, Griffin T W, Koh W J, Austin-Seymour M, Russell K J and Buchholz T A 1994 Fast neutron radiotherapy. The University of Washington experience *Acta Oncol.* **33** 275–80
Stewart R D, Yu V K, Georgakilas A G, Koumenis C, Park J H and Carlson D J 2011 Effects of radiation quality and oxygen on clustered DNA lesions and cell death *Radiat. Res.* **176** 587–602
Tobias C A 1985 The repair-misrepair model in radiobiology: comparison to other models *Radiat. Res. Suppl.* **8** S77–95
Tommasino F, Friedrich T, Scholz U, Taucher-Scholz G, Durante M and Scholz M 2013 A DNA double-strand break kinetic rejoining model based on the local effect model *Radiat. Res.* **180** 524–38
Tommasino F, Friedrich T, Scholz U, Taucher-Scholz G, Durante M and Scholz M 2015 Application of the local effect model to predict DNA double-strand break rejoining after photon and high-let irradiation *Radiat. Prot. Dosim.* **166** 66–70
Van den Heuvel F 2014 A closed parameterization of DNA-damage by charged particles, as a function of energy—a geometrical approach *PLoS One* **9** e110333
Wang C C, Hsiao Y, Lee C C, Chao T C and Tung C J 2012 Monte Carlo simulations of therapeutic proton beams for relative biological effectiveness of double-strand break *Int. J. Radiat. Biol.* **88** 158–63

Watanabe R, Rahmanian S and Nikjoo H 2015 Spectrum of radiation-induced clustered non-DSB damage—a Monte Carlo track structure modeling and calculations *Radiat Res* **183** 525–40

Worku M, Fersht N, Martindale C, Funes J M and Short S C 2013 Sequential transformation of mesenchymal stem cells is associated with increased radiosensitivity and reduced DNA repair capacity *Radiat. Res.* **179** 698–706

Wright E G 2010 Manifestations and mechanisms of non-targeted effects of ionizing radiation *Mutat. Res.* **687** 28–33

Wright E G and Coates P J 2006 Untargeted effects of ionizing radiation: implications for radiation pathology *Mutat. Res.* **597** 119–32

Yajima H, Fujisawa H, Nakajima N I, Hirakawa H, Jeggo P A, Okayasu R and Fujimori A 2013 The complexity of DNA double strand breaks is a critical factor enhancing end-resection *DNA Repair* (*Amst.*) **12** 936–46